Ascending Aortic Aneurysm in Angiotensin II–Infused Mice
Formation, Progression, and the Role of Focal Dissections

Bram Trachet, Alessandra Piersigilli, Rodrigo A. Fraga-Silva, Lydia Aslanidou, Jessica Sordet-Dessimoz, Alberto Astolfo, Marco F.M. Stampanoni, Patrick Segers, Nikolaos Stergiopulos

Objective—To understand the anatomy and physiology of ascending aortic aneurysms in angiotensin II–infused ApoE$^{-/-}$ mice.

Approach and Results—We combined an extensive in vivo imaging protocol (high-frequency ultrasound and contrast-enhanced microcomputed tomography at baseline and after 3, 10, 18, and 28 days of angiotensin II infusion) with synchrotron-based ultrahigh resolution ex vivo imaging (phase contrast X-ray tomographic microscopy) in n=47 angiotensin II–infused mice and 6 controls. Aortic regurgitation increased significantly over time, as did the luminal volume of the ascending aorta. In the samples that were scanned ex vivo, we observed one or several focal dissections, with the largest located in the outer convex aspect of the ascending aorta. The volume of the dissections moderately correlated to the volume of the aneurysm as measured in vivo (r^2=0.46). After 3 days of angiotensin II infusion, we found an interlaminar hematoma in 7/12 animals, which could be linked to an intimal tear. There was also a significant increase in single laminar ruptures, which may have facilitated a progressive enlargement of the focal dissections over time. At later time points, the hematoma was resorbed and the medial and adventitial thickness increased. Fatal transmural dissection occurred in 8/47 mice at an early stage of the disease, before adventita remodeling.

Conclusions—We visualized and quantified the dissections that lead to ascending aortic aneurysms in angiotensin II–infused mice and provided unique insight into the temporal evolution of these lesions. **(*Arterioscler Thromb Vasc Biol*. 2016;36:673-681. DOI: 10.1161/ATVBAHA.116.307211.)**

Key Words: aortic aneurysm ■ aortic dissection ■ ascending aorta ■ cardiovascular imaging ■ mouse models of human disease

Aortic aneurysm is clinically defined as a local increase in aortic diameter of at least 50% compared with the normal diameter.[1] Abdominal aortic aneurysms (AAA) are associated with cardiovascular risk factors, such as smoking, age, male sex, hyperlipidemia, hypertension, and chronic obstructive pulmonary disease.[2] Although these factors also underlie the majority of thoracic aortic aneurysms, the latter subgroup incidence is more often related to family history than to the above mentioned factors.[3] Because most aneurysms remain asymptomatic until—often fatal—complications such as rupture occur, our understanding of the pathogenesis, especially in early stages, is limited. Angiotensin II infusion into hypercholesterolemic ApoE$^{-/-}$ mice is a well-known experimental model of both AAAs[4] and thoracic aortic aneurysms.[5] We have recently explored a novel imaging technique, phase contrast X-ray tomographic microscopy (PCXTM), to visualize the abdominal lesions of angiotensin II–infused mice.[6] Because the axial resolution of our PCXTM scans (6.5 μm) was close to the thickness of histological coupes for routine morphological evaluation (4 μm), we introduced PCXTM-guided histology to select sections of the aorta in a highly precise manner for pathology analysis.[6] This approach allowed us to demonstrate that the abdominal lesions in these mice stem from medial ruptures in the suprarenal side branches, leading to media-adventitia dissection with intramural bleeding and thrombus formation.[6]

Much like in humans, data on thoracic aortic aneurysms are scarcer than data on AAAs in mouse models. Daugherty et al reported dilatation of the ascending aorta as semiquantified on histological sections after 28 days of continuous angiotensin II infusion in ApoE$^{-/-}$ mice.[5] They observed expansion of interlaminar spaces, collagen deposition, and macrophage

Received on: October 14, 2015; final version accepted on: February 5, 2016.

From the Institute of Bioengineering, Ecole Polytechnique Fédérale de Lausanne, Lausanne, Switzerland (B.T., R.A.F.-S., L.A., N.S.); IBiTech-bioMMeda, Ghent University-iMinds Medical IT, Ghent, Belgium (B.T., P.S.); School of Life Sciences, PTEC GE, Ecole Polytechnique Fédérale de Lausanne, Lausanne, Switzerland (A.P.); Institute of Animal Pathology, Vetsuisse Faculty, University of Bern, Bern, Switzerland (A.P.); Histology Core Facility, Ecole Polytechnique Fédérale de Lausanne, Lausanne, Switzerland (J.S.-D.); Swiss Light Source, Paul Scherrer Institut, Villigen, Switzerland (A.A., M.F.M.S.); and Institute for Biomedical Engineering, University and ETH Zürich, Zürich, Switzerland (M.F.M.S.).

The online-only Data Supplement is available with this article at http://atvb.ahajournals.org/lookup/suppl/doi:10.1161/ATVBAHA.116.307211/-/DC1.

Correspondence to Bram Trachet, LHTC STI IBI EPFL BM 5128 Station 17, CH-1015, Lausanne, Switzerland. E-mail bram.trachet@epfl.ch

Nonstandard Abbreviations and Acronyms	
2D	2-dimensional
3D	3-dimensional
AAA	abdominal aortic aneurysm
BMode	brightness mode
Micro-CT	microcomputed tomography
PCXTM	phase contrast X-ray tomographic microscopy

accumulation. The latter changes were found most extensively within the adventitia, whereas destruction of elastic fibers was observed on the outer convex aspect of the arch. Luminal dilatation,[7–9] wall thickening,[8,9] and elastin fragmentation[8,9] after 28 days of angiotensin II infusion were confirmed by other authors as well. Rateri et al reported a significant increase in diameter of the ascending aorta within 5 days using 2-dimensional (2D) high-frequency ultrasound. They also reported interlaminar hemorrhage at early time points.[9] Furthermore, they consistently observed mural medial breaks within the anterior aspects of the aorta.[9] Although detailed research on morphology, topography, and translational aspects of these ascending aorta lesions is still lacking, the mouse model is a common and convenient tool in preclinical pharmacological[10–13] and gene therapy[14] studies.

In the current article, we combined in vivo imaging with PCXTM and PCXTM-guided histology to visualize, characterize, and quantify the lesions in the ascending aorta of angiotensin II–infused ApoE$^{-/-}$ mice. We performed a longitudinal study with sacrifices at different time points and, hence, stages of disease development. A large number of lesions, particularly those found at the earliest time points, did not qualify as ascending aortic aneurysms from the pathomorphological point of view (not all layers were involved) nor the clinical point of view (no sufficient increase in lumen size). The study of these premature lesions with both established and novel technologies enabled us to present remarkable insights into the pathophysiology and morphology of murine ascending aortic aneurysms over time.

Materials and Methods

Materials and Methods are available in the online-only Data Supplement.

Results

Aortic Dimensions and Aortic Regurgitation

Using the clinical criterion of an increase in aortic size of 50%, 1/22 cases measured with motion mode (MMode) ultrasound, 3/27 cases measured with brightness mode (BMode) ultrasound, and 5/11 cases measured with microcomputed tomography (micro-CT) could be diagnosed with an ascending aortic aneurysm (comparing for each technique the aortic size at the latest available time point to the aortic size at baseline, in the animals that were scanned successfully at least twice). The ascending aorta diameter as measured with MMode (1-dimensional [1D]) increased significantly over time, but a statistically significant difference was only detected between baseline and day 28 (Figure 1E and Table I in the online-only Data Supplement). The aortic area as measured with longitudinal BMode (2D) and contrast-enhanced micro-CT (3-dimensional [3D]) increased highly significantly over time ($P<0.001$), and differences were significant in between intermediate time points as well (Figure 1F–1G; Table I in the online-only Data Supplement). Aortic regurgitation as quantified from pulsed Doppler measurements was present, but very low at baseline (day 0). Regurgitation was found to be significantly higher than baseline from day 10 onwards (Figure 1H; Table I in the online-only Data Supplement).

Wall Strain and Thickness

Circumferential Green-Lagrange strain decreased significantly over time ($P<0.001$). A sharp decrease occurred between baseline and day 3, after which the strain values stabilized (Figure 2B; Table I in the online-only Data Supplement). Both intima–media thickness and adventitial thickness as measured on Sirius Red–Miller stains were significantly different between angiotensin II–infused mice and controls (Table I in the online-only Data Supplement). The medial thickness only reached a significant difference after 28 days (Figure 2C), whereas the adventitial thickness was already significantly different from saline-infused controls at day 10 (Figure 2D). There was also a trend for increased collagen content in the wall ($P=0.51$; Table I in the online-only Data Supplement; Figure 2E).

Focal Dissections in the Ascending Aorta

In n=41/42 scanned samples, the ex vivo PCXTM images revealed at least 1 and maximum 4 dissections, defined as gaps in the aortic wall of at least 10% of the local wall thickness (Figure 3A). The geometric mean of the dissection length was 1.07 mm per sample (95% confidence interval: 0.81–1.41), its wall surface area was 0.97 mm^2 (95% confidence interval: 0.65–1.46), and its wall volume was 0.022 mm^3 (95% confidence interval: 0.013–0.037). No dissections were observed in control animals. Although the largest dissections occurred at the latest time points, no significant difference in lesion volume was observed between the investigated time points of angiotensin II infusion (Figure 3B; Table I in the online-only Data Supplement). There was a significant difference in dissection incidence and dissection size in between circumferential quadrants. The lowest number of dissections occurred on the inner convex aspect of the aorta, with pairwise comparisons being significant between the inner convex and right aspects (Figure 3C; Table II in the online-only Data Supplement). The largest dissections occurred on the outer convex quadrant of the aorta, with pairwise comparisons being significant between the outer convex and left quadrants (Figure 3C; Table I in the online-only Data Supplement). The volume of the ascending aorta as measured with micro-CT before killing (Figure 1C, red) correlated moderately ($r^2=0.46$) with the volume of the dissections (Figure 3A, orange; Figure 3D).

The dissections were characterized on image-guided histology by a loss of continuity in at least 3 adjacent inner elastic laminae of the tunica media (Figure 4A and 4C). Applying the morpho-pathological criterion for an aneurysm (ie, a vascular outpouch involving all layers of the wall[15]), one could state that only 54% of the investigated stains that showed (part of)

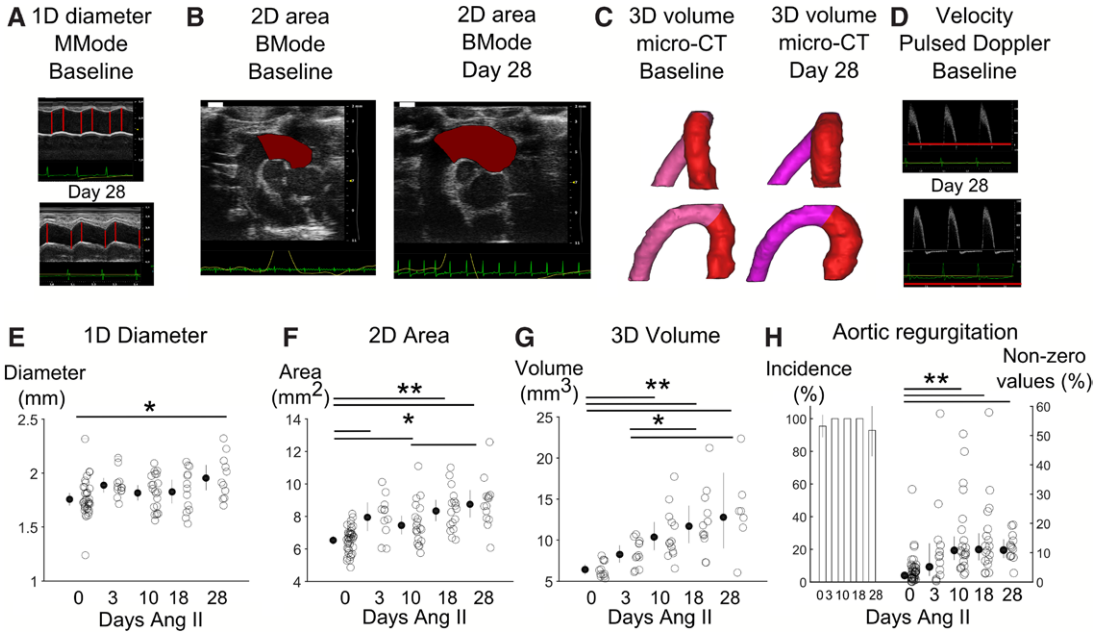

Figure 1. In vivo changes in aortic size and aortic regurgitation severity. **Top**, Representative images of in vivo acquisition of size and blood velocity of the ascending aorta with 1-dimensional (1D) motion mode (MMode; **A**), 2-dimensional (2D) brightness mode (BMode; **B**), 3-dimensional (3D) microcomputed tomography (micro-CT; **C**), and pulsed Doppler (**D**). Measured regions are shown in red. Scale bar represents 1 mm. **E–G**, Scatter plots show the measurements at different time points (1D, MMode; 2D, BMode; 3D, micro-CT), as well as the mean and the 95% confidence interval (calculated in the normal domain after a log transformation). **H,** The bar plots (**left**) show the incidence of aortic regurgitation for each time point (100×n1/n2; n1, all mice that have aortic regurgitation at that time point; and n2, all mice measured at that time point), whereas the scatter plots (**right**) show the amount of regurgitation in those mice where aortic regurgitation was present (nonzero values). *P<0.05, **P<0.001.

a dissection had developed a true ascending aortic aneurysm (Figure 4B). Apoptosis of smooth muscle cells was most outspoken at the latest time points and at the edges of the dissection (Figure IA in the online-only Data Supplement). The remaining, intact segments of the vessel did not exhibit evidence of ongoing apoptosis.

Interlaminar Microhemorrhage

H&E stained sections showed that interlaminar microhemorrhages and hematomas occurred after 3 days of angiotensin II infusion (Figure 5A). The hematoma size as measured on HE stains was larger after 3 days of angiotensin II infusion than at subsequent time points, indicating this lesion to be an early step

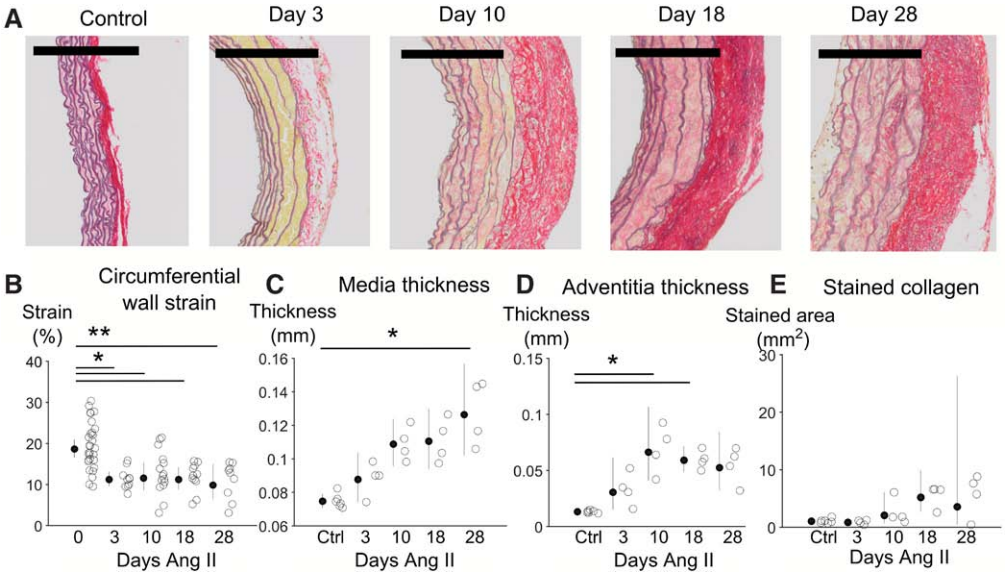

Figure 2. Spatial and temporal variation of aortic wall properties and morphology. **Top**, Representative Sirius Red–Miller stains showing the aortic wall matrix composition at different time points; collagen in red and elastin in grey. Scale bar represents 200 μm. **B–E**, Scatter plots show the evolution of circumferential strain (**B**), intima–media thickness (**C**), adventitia thickness (**D**), and collagen deposition (**E**) over time. The mean and 95% confidence interval are calculated in the normal domain after a log transformation. Three to 4 stains, each obtained by image-guided histology, were averaged per animal to account for intrasubject variation. *P<0.05, **P<0.001.

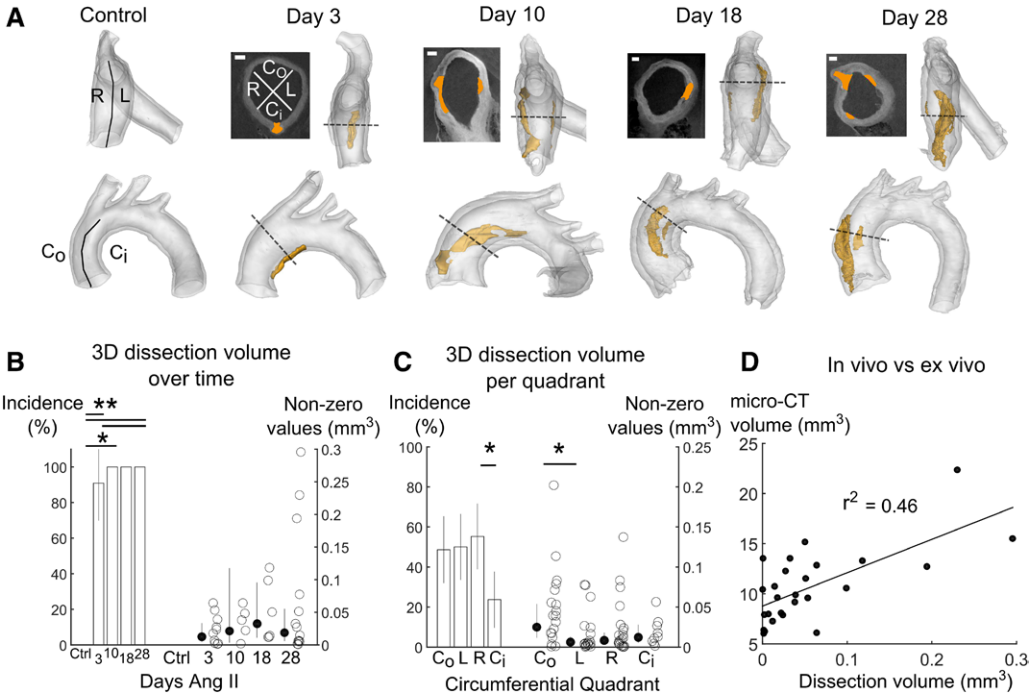

Figure 3. Three dimensional (3D) phase contrast X-ray tomographic microscopy (PCXTM) imaging of focal dissections. **A**, Two-dimensional (2D) and segmented 3D representation of the aortic arch at different time points. Dissections in orange. C_o indicates outer convex quadrant; C_i, inner convex quadrant; L, left quadrant; and R, right quadrant. Scale bar represents 200 μm. **B**, PCXTM-based dissection volume over time. The bar plots (**left**) show the incidence of aortic dissections for each time point (100×n1/n2; n1, all mice that have a dissection at that time point; and n2, all mice measured at that time point), whereas the scatter plots (**right**) show the volume of the dissections for the nonzero values (n1). **C**, PCXTM-based dissection volume over the circumference. The bar plots (**left**) show the incidence of aortic dissections in each quadrant, whereas the scatter plots (**right**) show the volume of the dissections for the nonzero values. **D**, Scatter plot showing the relation between lumen volume obtained with in vivo microcomputed tomography (micro-CT; Figure 1C, red volume) and dissection volume obtained with ex vivo PCXTM (Figure 3A, orange volume). **P*<0.05, ***P*<0.001.

in the pathogenesis of aneurysms in mice (Figure 5C; Table I in the online-only Data Supplement). The accumulation of extraluminal free erythrocytes occurred more frequently in the outer (abluminal) laminae (L4–L7); no hematoma was found in the inner 2 laminae (L1–L2; Figure 5D; Table II in the online-only Data Supplement). Hemosiderophages, stained with Prussian blue, were seen resorbing the hematoma at later time points (Figure IB in the online-only Data Supplement). These observations were confirmed on the 3D PCXTM images of the animals that had been scanned with contrast-enhanced micro-CT (Figure 5B). The incidence of extraluminal, intramural Exitron leakage (Exitron is the micro-CT contrast agent that had been injected in vivo) was significantly higher after 3 days of angiotensin II infusion than for controls. At later time points, the difference was no longer significant (Figure 5E; Table I in the online-only Data Supplement).

Elastic Laminae Ruptures

The combined Sirius Red–Miller stained slides revealed several discrete discontinuities in the medial (elastic) laminae (Figure 6A). Laminar ruptures were present in all animals (Figure 6B; Table II in the online-only Data Supplement). The total number of laminar ruptures was significantly higher in angiotensin II–infused animals than in controls (Table I in the online-only Data Supplement). The difference reached significance after 18 days of Ang II infusion (Figure 6B). Neither the incidence nor the number of ruptures varied in between different quadrants (Figure 6C; Tables I and II in the online-only Data Supplement). However, both the incidence and the number of ruptures were significantly different in between layers. The highest number of laminar ruptures occurred in the central laminae (L2–L4), whereas the outer laminae (L1, L7) were less frequently affected (Figure 6D and Tables I and II in the online-only Data Supplement).

Transmural Dissection

All of the 8 animals that were found dead in their cage with hemothorax had died between 3 and 8 days of angiotensin II infusion, during the initial stage of disease development. Six out of these 8 ascending aortic samples were scanned ex vivo with PCXTM. In all 6 cases, the cause of death could be related to a hemothorax, secondary to the transmural dissection of the ascending aortic wall. PCXTM-guided histology confirmed a complete rupture of all laminae in the tunica media. The transmural dissection ran in the cranial direction (toward the aortic root), be it on the inner convex aspect (Figure IIA in the online-only Data Supplement) or on the outer convex aspect (Figure IIC in the online-only Data Supplement) of the aorta.

Discussion

In Vivo and Ex Vivo Imaging: Interpreting the Observations

To the best of our knowledge, our ex vivo PCXTM images are the first report of volume and location of the focal dissections

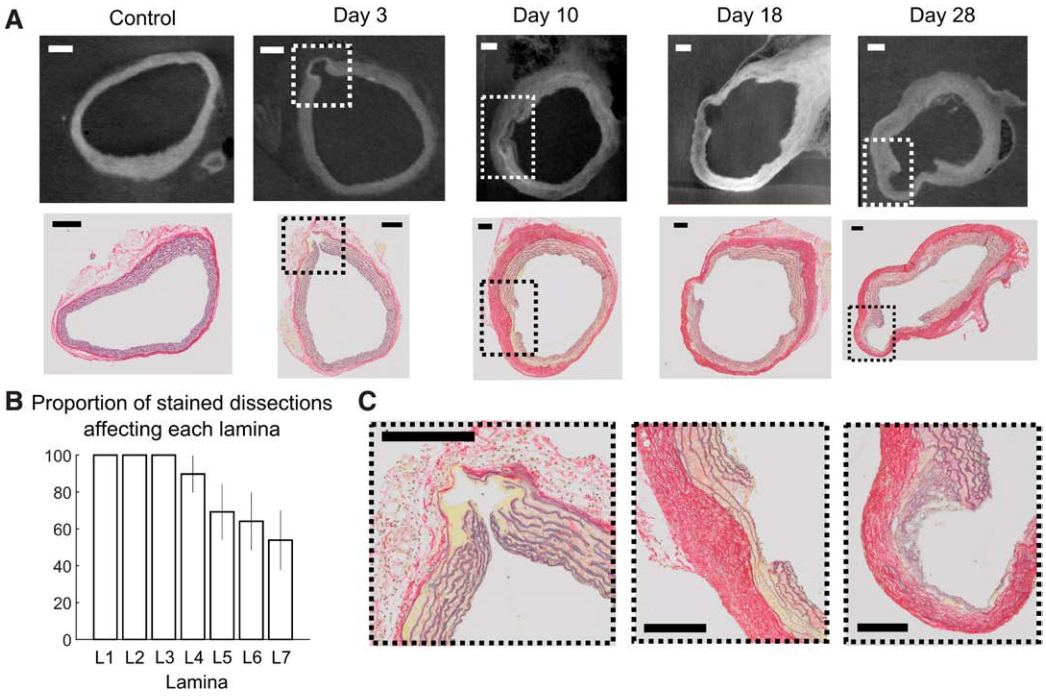

Figure 4. Two-dimensional (2D) phase contrast X-ray tomographic microscopy (PCXTM) and Sirius Red (SR)–Miller stains of focal dissections. **A**, **Top**, 2D PCXTM images of focal dissections at different time points. **Bottom**, PCXTM-guided SR-Miller stains of focal dissections at sections corresponding to the images on top. Scale bar represents 200 μm. **B,** Bar plot indicating the percentage (and 95% confidence interval) of stained dissections in which each lamina was found to be ruptured, relative to the total number of stains in which (part of) a dissection was visible. The total number of stains was obtained across all investigated time points. L1 indicates luminal (intima); and L7, abluminal (adjacent to adventitia). **C**, Zoomed sections of (**A**). **Left**, A stained dissection in which all laminae (L1–L7) were affected. **Right**, A stained dissection in which only the inner laminae (L1–L4) were affected.

that cause ascending aortic aneurysms in angiotensin II–infused mice. Despite the focal and asymmetrical nature of the wall damage observed ex vivo, an asymmetrical outpouch with luminal expansion was not observed in vivo with BMode or micro-CT. Nevertheless, the luminal volume observed with micro-CT just before killing correlated moderately with the size of the focal dissections observed with PCXTM (r^2=0.46; Figure 3D). Because the size of the dissections was quantified in the absence of intra-aortic pressure, this correlation does not account for the impact of the dissection on the structural properties and strain of the aorta. Moreover, the size of the aneurysm might also be influenced by wall remodeling (Figure 2), intramural hematoma formation (Figure 5), and discrete laminar ruptures (Figure 6), all of which affect the entire wall and not just the region of the dissection. Considering these confounding factors, we think that a correlation of r^2=0.46 is not insignificant and that our data support a (possibly indirect) relationship between the size of the observed dissections and the size of the aneurysm in vivo.

Within the different in vivo imaging techniques, the increased accuracy and added information of 2D BMode and especially 3D micro-CT resulted in more overt, more gradual, and more significant differences in between different time points than what was obtained with 1D MMode (Figure 1E–1G; Table I in the online-only Data Supplement). Our data thus contradict earlier findings of Rateri et al, who observed a more gradual increase with 1D MMode than with 2D BMode, whereas their BMode measurements reached a plateau value after 7 days of angiotensin II infusion.[9] Moreover, 3D imaging enabled us to identify aneurysms that were not picked up by 2D, and 2D imaging was more sensitive than 1D. Because 1D and 2D ultrasound strongly depend on the field of view chosen by the user,[16] these findings indicate that for follow-up studies on aneurysm formation, 3D images should be acquired when possible.

Both aortic regurgitation and ascending aortic volume were significantly increased after 10 days of angiotensin II infusion (Figure 1G–1H). This leads to a dilemma that has also been discussed in a clinical context: did the dilatation of the aorta cause the regurgitation or vice versa?[17,18] On the one hand, fast progression of the disease (both variables were already increased, albeit not significantly, after 3 days) seems to suggest that in angiotensin II–infused mice, diastolic regurgitation was the consequence rather than the cause of aortic dilatation, most likely driven by poor leaflet coaptation.[19] On the other hand, once present, diastolic backflow and the subsequent hemodynamic perturbations might have played an important role in the further degeneration of the wall.[20] This is further supported by the fact that the volume of the dissections was larger in the most convex aspect of the aorta (Figure 3C). Aortic regurgitation has been reported to induce aortic remodeling in the outer convex aspect of the ascending aorta in pigs.[21] In human patients with a bicuspid valve, aortic expansion[22] and extracellular matrix protein expression[17] were also increased in the most convex part of the ascending aorta. The latter might thus be a locus minoris resistentiae to hemodynamic alterations. Follow-up research is needed to provide more insight into the intriguing role of aortic regurgitation in this mouse model.

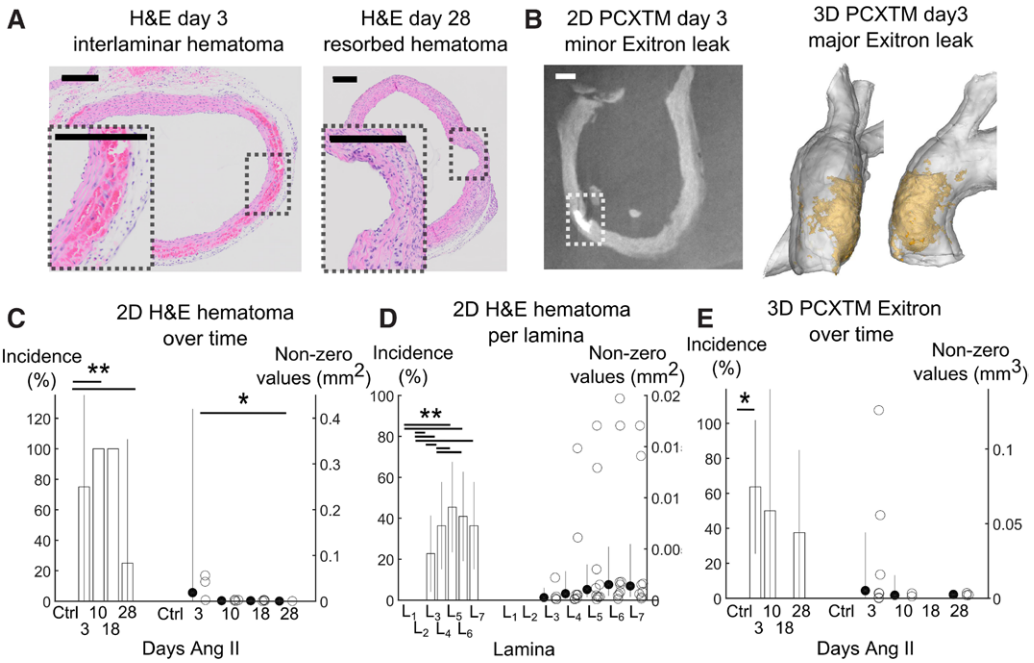

Figure 5. Spatial and temporal distribution of interlaminar hematoma. **A,** Representative Hematoxin–Eosin (H&E) stains after 3 and 28 days of angiotensin II infusion. Scale bar represents 200 μm. **B**, **Left**, Two-dimensional (2D) phase contrast X-ray tomographic microscopy (PCXTM) image showing how Exitron (white contrast agent, injected in vivo before killing) leaks in between the laminae through an intimal tear. **Right**, Three-dimensional (3D) representation of a major Exitron leakage (in orange) that has percolated into the tunica media (in transparent white). **C**, Change in hematoma area over time. The bar plots (**left**) show the incidence of hematoma on the analyzed stains at each time point, whereas the scatter plots (**right**) show the area of the hematoma for nonzero values. **D**, Change in hematoma area per lamina. Three to 4 stains, each obtained by image-guided histology, were averaged per animal to account for intrasubject variation. **E**, Exitron volume penetrating into the tunica media over time. **P*<0.05, ***P*<0.001.

Image-Guided Histology: Exploring Potential Mechanisms

Because the paraffin cutting (before staining) was guided by the PCXTM images, we were able to target the exact region of interest within each analyzed lesion. The analysis of this image-guided histology revealed significant differences between early and late time points of angiotensin II infusion.

We observed large intramural hematomas after only 3 days of angiotensin II infusion (Figure 5). The presence of Exitron aggregates within the wall indicates an intra vitam locally increased permeability of the vessel wall or even loss of continuity of the endothelial lining.[6] In contrast to Rateri et al, who could not identify any access point for the interlaminar hematoma,[9] PCXTM- (Figure 5B) and PCXTM-guided histology (Figure 4A, day 3) allowed us to visualize the intimal defect which led to a mural bleeding at these early time points.

We also found an increase in laminar ruptures in the tunica media at an early stage of the disease (Figure 6). Because these laminar ruptures were highly frequent in the second and third lamina (Figure 6D), both of which were affected in all focal dissections (Figure 4B), one might hypothesize that the dissections were the result of a progressive tear that had been initiated by a combination of single laminar ruptures. This theory is further supported by the anecdotal observation that 7/41 focal dissections occurred in bilateral pairs, with a tear on the right side of the aorta accompanied by a mirroring one on the left (eg, Figure 3A, day 10–18 and Figure 4A, day18). If several laminar ruptures culminate into a dissection on one side (left or right), this might locally elongate the aorta and increase the tension on the other side, thus leading to additional laminar ruptures on that side and an ipsilateral, symmetrical dissection.

Because apoptosis was mainly observed at later time points and near the edge of dissections (Figure IA in the online-only Data Supplement), it may have played an important role in the progressive enlargement of the lesion over time, rather than being an early event as widely assumed.[23] The progression over time of an initially small tear could also be driven by mechanical forces and factors, such as the loss of recoil of adjacent intact elastic laminae, the focal loss of vessel wall compliance (as evidenced by a decrease in circumferential strain, Figure 2B), and interlaminar bleeding (Figure 5).

After the initial events, further degradation occurred, and medial elements were replaced by the deposition of collagen in response to hematoma organization and remodeling of the vessel wall (Figure 2A). Because the medial thickness did not change much after day 10 (Figure 2C), we hypothesize that the formation of granulation tissue (at first) and fibrosis (later on) were counterbalanced by compensatory hypertrophy and hyperplasia of the remaining medial smooth muscle cells. This could trigger a vicious circle of degeneration, loss, and switch of the contractile phenotype for a secretory one.[24] The altered physical properties of the wall possibly predisposed other sectors of the segment to undergo degenerative medial changes as well.

We think that the changes in the adventitia were the result of a combined effect of (1) systemic angiotensin II–induced vessel fibrosis[25] and (2) local reinforcement of the adventitia

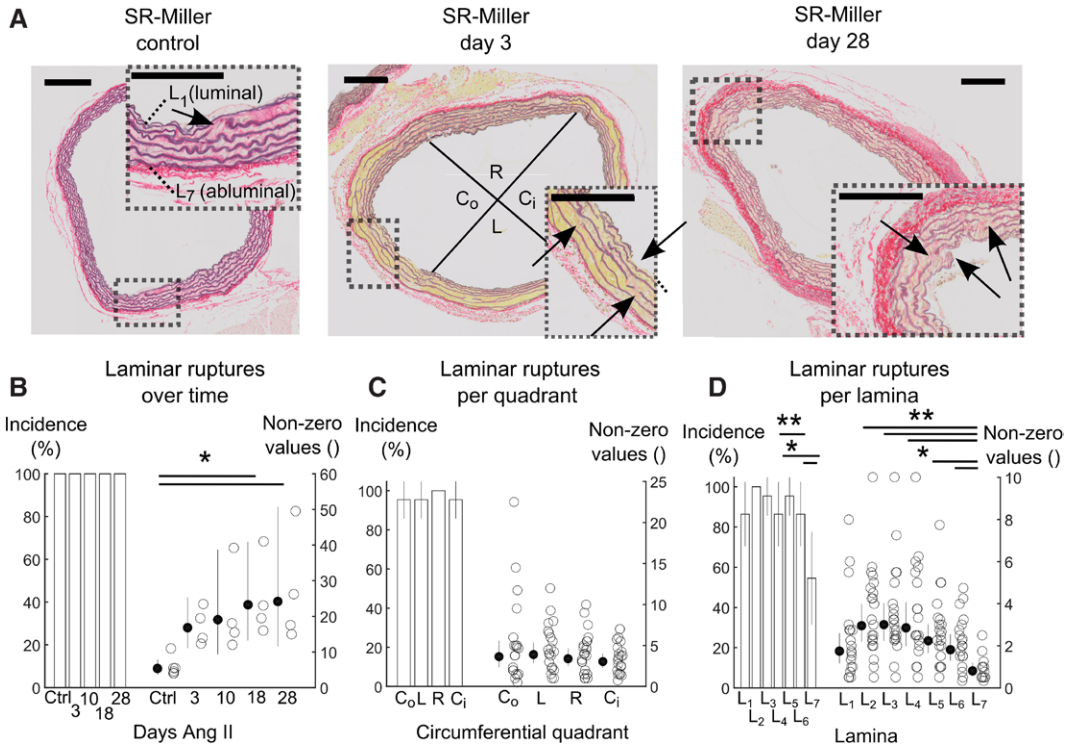

Figure 6. Spatial and temporal distribution of laminar ruptures. **A**, Representative Sirius Red (SR)–Miller stains showing elastic laminae ruptures after saline infusion (**left**) and after 3 (**middle**) and 28 (**right**) days of angiotensin II infusion. Laminar ruptures that were part of focal dissections were not taken into account to avoid double reporting. Scale bar represents 200 μm. **B**, Laminar ruptures over time. The bar plots (**left**) show the incidence of laminar ruptures at each time point, whereas the scatter plots (**right**) show the number of ruptures for each time point. **C,** Circumferential variation of laminar ruptures. **D**, Change in laminar ruptures per lamina. L1 indicates luminal (intima); and L7, abluminal (adjacent to adventitia). Three to 4 stains, each obtained by image-guided histology, were averaged per animal to account for intrasubject variation. *P<0.05, **P<0.001.

near focal dissections to prevent transmural dissection as a result of the locally weakened tunica media. The latter is further supported by the fact that all fatal transmural dissections occurred after 4.6±1.8 days of angiotensin II infusion (Figure II in the online-only Data Supplement), when adventitial remodeling was still at a premature stage (Figure 2D–2E). A transmural dissection may have occurred in those cases where the focal dissection evolved too abruptly, so that the outer wall segments (which did not have the time to remodel) could not bear the increased load.

Translational Value of the Mouse Model

Our previously published PCXTM findings discussed morphological differences between dissecting AAAs in angiotensin II–infused mice and AAAs observed in humans.[6] The focal and partial dissections of the tunica media that we report here have, to the best of our knowledge, never been reported in humans. However, ex vivo images that visualize the entire ascending aortic wall in 3D with a superior resolution are difficult (if not impossible) to obtain in a clinical context. Therefore, final conclusions about the translational value of the ascending aneurysms in this mouse model are premature at this stage.

An important difference between mice and men is the number of laminae in the tunica media (±7 in mice and ±50 in humans[26]). Wolinsky and Glagov stated that the tension per lamellar unit is constant (2 N/m) among species,[27] but this was later disputed by Shadwick.[28] Hence, the tension on each lamina might be higher in mice. Also, in mice, a rupture in one lamina will have a greater impact on the local load-bearing capacity, and the tension on the remaining laminae will be higher. This might explain the observed focal nature of the dissections in mice and the fast evolution of the disease compared with that in humans. A detailed computational analysis would be necessary to confirm this hypothesis.[29]

Limitations and Future Work

In this study, baseline measurements (before pump implantation) were used as controls for in vivo experiments (ultrasound, micro-CT), whereas saline-infused ApoE$^{-/-}$ mice were used as controls for the ex vivo experiments (PCXTM, histology). We did not investigate the influence of hyperlipidemia on ascending aortic aneurysm formation in this mouse model, and we did not use age-matched controls. These choices were based on the 3R principle (reducing the number of experimental animals as much as possible) and on previous studies reporting negative controls at different time points.[8,9,13] Nevertheless, we cannot completely exclude the possibility that the inclusion of normolipidemic mice or age-matched controls would have affected the conclusions of our work.

We could not find an unequivocal explanation as to why the hematoma was restricted to the outer laminae. We hypothesize that an interstitial outward pressure gradient might be present within the tunica media. Nevertheless, we

cannot exclude the possibility that the hematoma was not just caused by an intimal tear and that additional breaches exist in the outer layers. This theory is supported by the fact that in 3/42 scanned samples, a focal hematoma was detected at the level of the aortic arch. Because there was no intimal tear in these cases, these hematomas possibly originated from ruptured vasa vasorum in the outer laminae of the tunica media (Figure IIC in the online-only Data Supplement).

Although the largest dissections were found at the latest time point, we did not find a statistically significant increase in dissection size over time. The reason is that a considerable number of animals only had small dissections (Figure 3B) or less prominent adventitial remodeling (Figure 2D–2E). A similar variability in size and timing of the lesions have previously been observed in dissecting AAAs in this mouse model.[30] This is relatively surprising given the homogeneity of the genetic background in inbred mice and the identical environmental and experimental conditions and may be related to epigenetic heterogeneity or differences in local hemodynamics. Such factors should be taken into account and, if possible, further elucidated for future studies to empower this model.

Conclusions

We investigated the pathogenesis of ascending aortic aneurysms in angiotensin II–infused mice by longitudinal in vivo monitoring as well as ex vivo synchrotron-based imaging and image-guided histology of the vessel. We visualized how the axisymmetric increase in luminal size that was measured in vivo was related to highly nonsymmetrical focal dissections within the aneurysm wall and explored potential disease mechanisms. These novel insights into the morphological pathology of the aortic wall in ascending aneurysms of angiotensin II–infused mice will help to interpret treatment studies using this mouse model, both prospectively and retrospectively.

Acknowledgments

We thank Dr Pablo Villanueva, Dr Orestis Vardoulis, Dr Carole Van der Donckt, and Bieke Vanderveken for their assistance during the PCXTM scans. Further, we wish to acknowledge Agnès Hautier and the entire team of the Histology Core Facility at Ecole Polytechnique Fédérale de Lausanne (EPFL) for their technical expertise with the PCXTM-guided histology and José Artacho from the Bioimaging and Optics platform at EPFL for his help with the image data acquisition. We also thank Marion Varet, Celine Waldvogel, and the entire team of the Phenotyping Unit in the Center of PhenoGenomics at the school of Life Sciences in EPFL for their technical and scientific expertise in the micro-CT experiments. Finally, we thank Dr Philippe Jacquet of the Statistics Core Facility at EPFL for his expert help in organizing the data and Dr Massimiliano Mariani and Dr Julie De Backer for their clinical input and revision of the article.

Sources of Funding

This research was funded by the Special Research Fund of Ghent University and by internal funds of the Laboratory of Hemodynamics and Cardiovascular Technology, EPFL.

Disclosures

None.

References

1. Alexander JJ. The pathobiology of aortic aneurysms. *J Surg Res*. 2004;117:163–175. doi: 10.1016/j.jss.2003.11.011.
2. Sakalihasan N, Limet R, Defawe OD. Abdominal aortic aneurysm. *Lancet*. 2005;365:1577–1589. doi: 10.1016/S0140-6736(05)66459-8.
3. Coady MA, Davies RR, Roberts M, Goldstein LJ, Rogalski MJ, Rizzo JA, Hammond GL, Kopf GS, Elefteriades JA. Familial patterns of thoracic aortic aneurysms. *Arch Surg*. 1999;134:361–367.
4. Daugherty A, Manning MW, Cassis LA. Angiotensin II promotes atherosclerotic lesions and aneurysms in apolipoprotein E-deficient mice. *J Clin Invest*. 2000;105:1605–1612. doi: 10.1172/JCI7818.
5. Daugherty A, Rateri DL, Charo IF, Owens AP, Howatt DA, Cassis LA. Angiotensin II infusion promotes ascending aortic aneurysms: attenuation by CCR2 deficiency in apoE-/- mice. *Clin Sci (Lond)*. 2010;118:681–689. doi: 10.1042/CS20090372.
6. Trachet B, Fraga-Silva RA, Piersigilli A, Tedgui A, Sordet-Dessimoz J, Astolfo A, Van der Donckt C, Modregger P, Stampanoni MF, Segers P, Stergiopulos N. Dissecting abdominal aortic aneurysm in Ang II-infused mice: suprarenal branch ruptures and apparent luminal dilatation. *Cardiovasc Res*. 2015;105:213–222. doi: 10.1093/cvr/cvu257.
7. Favreau JT, Nguyen BT, Gao I, Yu P, Tao M, Schneiderman J, Gaudette GR, Ozaki CK. Murine ultrasound imaging for circumferential strain analyses in the angiotensin II abdominal aortic aneurysm model. *J Vasc Surg*. 2012;56:462–469. doi: 10.1016/j.jvs.2012.01.056.
8. Branchetti E, Poggio P, Sainger R, Shang E, Grau JB, Jackson BM, Lai EK, Parmacek MS, Gorman RC, Gorman JH, Bavaria JE, Ferrari G. Oxidative stress modulates vascular smooth muscle cell phenotype via CTGF in thoracic aortic aneurysm. *Cardiovasc Res*. 2013;100:316–324. doi: 10.1093/cvr/cvt205.
9. Rateri DL, Davis FM, Balakrishnan A, Howatt DA, Moorleghen JJ, O'Connor WN, Charnigo R, Cassis LA, Daugherty A. Angiotensin II induces region-specific medial disruption during evolution of ascending aortic aneurysms. *Am J Pathol*. 2014;184:2586–2595. doi: 10.1016/j.ajpath.2014.05.014.
10. Chen X, Rateri DL, Howatt DA, Balakrishnan A, Moorleghen JJ, Morris AJ, Charnigo R, Cassis LA, Daugherty A. Amlodipine reduces AngII-induced aortic aneurysms and atherosclerosis in hypercholesterolemic mice. *PLoS One*. 2013;8:e81743. doi: 10.1371/journal.pone.0081743.
11. Subramanian V, Moorleghen JJ, Balakrishnan A, Howatt DA, Chishti AH, Uchida HA. Calpain-2 compensation promotes angiotensin II-induced ascending and abdominal aortic aneurysms in calpain-1 deficient mice. *PLoS One*. 2013;8:e72214. doi: 10.1371/journal.pone.0072214.
12. Zhang X, Thatcher SE, Rateri DL, Bruemmer D, Charnigo R, Daugherty A, Cassis LA. Transient exposure of neonatal female mice to testosterone abrogates the sexual dimorphism of abdominal aortic aneurysms. *Circ Res*. 2012;110:e73–e85. doi: 10.1161/CIRCRESAHA.111.253880.
13. Fu XM, Yamawaki-Ogata A, Oshima H, Ueda Y, Usui A, Narita Y. Intravenous administration of mesenchymal stem cells prevents angiotensin II-induced aortic aneurysm formation in apolipoprotein E-deficient mouse. *J Transl Med*. 2013;11:175. doi: 10.1186/1479-5876-11-175.
14. Rateri DL, Moorleghen JJ, Balakrishnan A, Owens AP III, Howatt DA, Subramanian V, Poduri A, Charnigo R, Cassis LA, Daugherty A. Endothelial cell-specific deficiency of Ang II type 1a receptors attenuates Ang II-induced ascending aortic aneurysms in LDL receptor-/- mice. *Circ Res*. 2011;108:574–581. doi: 10.1161/CIRCRESAHA.110.222844.
15. McGavin MD, Zachary JF. *Pathologic Basis of Veterinary Disease, 4th ed*. Missouri: Mosby Elsevier; 2007.
16. Trachet B, Fraga-Silva RA, Londono FJ, Swillens A, Stergiopulos N, Segers P. Performance comparison of ultrasound-based methods to assess aortic diameter and stiffness in normal and aneurysmal mice. *PLoS One*. 2015;10:e0129007. doi: 10.1371/journal.pone.0129007.
17. Cotrufo M, Della Corte A, De Santo LS, Quarto C, De Feo M, Romano G, Amarelli C, Scardone M, Di Meglio F, Guerra G, Scarano M, Vitale S, Castaldo C, Montagnani S. Different patterns of extracellular matrix protein expression in the convexity and the concavity of the dilated aorta with bicuspid aortic valve: preliminary results. *J Thorac Cardiovasc Surg*. 2005;130:504–511. doi: 10.1016/j.jtcvs.2005.01.016.
18. Bissell MM, Hess AT, Biasiolli L, Glaze SJ, Loudon M, Pitcher A, Davis A, Prendergast B, Markl M, Barker AJ, Neubauer S, Myerson SG. Aortic dilation in bicuspid aortic valve disease: flow pattern is a major contributor and differs with valve fusion type. *Circ Cardiovasc Imaging*. 2013;6:499–507. doi: 10.1161/CIRCIMAGING.113.000528.
19. Tadros TM, Klein MD, Shapira OM. Ascending aortic dilatation associated with bicuspid aortic valve: pathophysiology, molecular biology,

and clinical implications. *Circulation*. 2009;119:880–890. doi: 10.1161/CIRCULATIONAHA.108.795401.
20. Zhou YQ, Zhu SN, Foster FS, Cybulsky MI, Henkelman RM. Aortic regurgitation dramatically alters the distribution of atherosclerotic lesions and enhances atherogenesis in mice. *Arterioscler Thromb Vasc Biol*. 2010;30:1181–1188. doi: 10.1161/ATVBAHA.110.204198.
21. Atkins SK, Cao K, Rajamannan NM, Sucosky P. Bicuspid aortic valve hemodynamics induces abnormal medial remodeling in the convexity of porcine ascending aortas. *Biomech Model Mechanobiol*. 2014;13:1209–1225. doi: 10.1007/s10237-014-0567-7.
22. Cotrufo M, Della Corte A. The association of bicuspid aortic valve disease with asymmetric dilatation of the tubular ascending aorta: identification of a definite syndrome. *J Cardiovasc Med (Hagerstown)*. 2009;10:291–297. doi: 10.2459/JCM.0b013e3283217e29.
23. Durdu S, Deniz GC, Balci D, Zaim C, Dogan A, Can A, Akcali KC, Akar AR. Apoptotic vascular smooth muscle cell depletion via BCL2 family of proteins in human ascending aortic aneurysm and dissection. *Cardiovasc Ther*. 2012;30:308–316. doi: 10.1111/1755-5922.12007.
24. Lesauskaite V, Tanganelli P, Sassi C, Neri E, Diciolla F, Ivanoviene L, Epistolato MC, Lalinga AV, Alessandrini C, Spina D. Smooth muscle cells of the media in the dilatative pathology of ascending thoracic aorta: morphology, immunoreactivity for osteopontin, matrix metalloproteinases, and their inhibitors. *Hum Pathol*. 2001;32:1003–1011. doi: 10.1053/hupa.2001.27107.
25. van Thiel BS, van der Pluijm I, te Riet L, Essers J, Danser AH. The renin-angiotensin system and its involvement in vascular disease. *Eur J Pharmacol*. 2015;763(pt A):3–14. doi: 10.1016/j.ejphar.2015.03.090.
26. van Thiel BS, van der Pluijm I, te Riet L, Essers J, Danser AH. The renin-angiotensin system and its involvement in vascular disease. *Eur J Pharmacol*. 2015;763(Pt A):3–14. doi: 10.1016/j.ejphar.2015.03.090.
27. Wolinsky H, Glagov S. Structural basis for the static mechanical properties of the aortic media. *Circ Res*. 1964;14:400–413.
28. Shadwick RE. Mechanical design in arteries. *J Exp Biol*. 1999;202(Pt 23):3305–3313.
29. Trachet B, Bols J, Degroote J, Verhegghe B, Stergiopulos N, Vierendeels J, Segers P. An animal-specific FSI model of the abdominal aorta in anesthetized mice. *Ann Biomed Eng*. 2015;43:1298–1309. doi: 10.1007/s10439-015-1310-y.
30. Trachet B, Fraga-Silva RA, Jacquet PA, Stergiopulos N, Segers P. Incidence, severity, mortality, and confounding factors for dissecting AAA detection in angiotensin II-infused mice: a meta-analysis. *Cardiovasc Res*. 2015;108:159–170. doi: 10.1093/cvr/cvv215.

Significance

Angiotensin II–infused ApoE$^{-/-}$ mice are an important mouse model for aortic aneurysm, but the anatomy of their ascending aneurysms has never been fully understood because of inherent limitations in the currently available small animal imaging technology. In this work, we combined in vivo imaging with high-resolution ex vivo imaging and image-guided histology to provide an unprecedented insight into the pathophysiology and the temporal evolution of these lesions. In the short term, our aim is to improve the basic knowledge of how ascending aortic aneurysms form in mice and to serve as a valuable source of insight for past and future studies that rely on this popular mouse model. In the long term, we think that our research will improve future preclinical aneurysm research and that it will contribute to enhance our understanding of the initiation of ascending aortic aneurysm in humans.

Arteriosclerosis, Thrombosis, and Vascular Biology

JOURNAL OF THE AMERICAN HEART ASSOCIATION

Ascending Aortic Aneurysm in Angiotensin II–Infused Mice: Formation, Progression, and the Role of Focal Dissections

Bram Trachet, Alessandra Piersigilli, Rodrigo A. Fraga-Silva, Lydia Aslanidou, Jessica Sordet-Dessimoz, Alberto Astolfo, Marco F.M. Stampanoni, Patrick Segers and Nikolaos Stergiopulos

Arterioscler Thromb Vasc Biol. 2016;36:673-681; originally published online February 18, 2016;
doi: 10.1161/ATVBAHA.116.307211
Arteriosclerosis, Thrombosis, and Vascular Biology is published by the American Heart Association, 7272 Greenville Avenue, Dallas, TX 75231

Print ISSN: 1079-5642. Online ISSN: 1524-4636

Ascending aortic aneurysm in angiotensin II- infused mice: formation, progression and the role of focal dissections

Supplementary Data:

Detailed Materials and Methods

Bram Trachet[1,2], Alessandra Piersigilli[3,4], Rodrigo A. Fraga-Silva[1], Lydia Aslanidou[1], Jessica Sordet-Dessimoz[5], Alberto Astolfo[6], Marco F.M. Stampanoni[6,7], Patrick Segers[2], Nikolaos Stergiopulos[1]

[1] Institute of Bioengineering, Ecole Polytechnique Fédérale de Lausanne, Lausanne, Switzerland

[2] IBiTech - bioMMeda, Ghent University-iMinds Medical IT, Ghent, Belgium

[3] School of Life Sciences, PTEC GE, Ecole Polytechnique Fédérale de Lausanne, Lausanne, Switzerland

[4] Institute of Animal Pathology, Vetsuisse Faculty, University of Bern, Bern, Switzerland

[5] Histology Core Facility, Ecole Polytechnique Fédérale de Lausanne, Lausanne, Switzerland

[6] Swiss Light Source, Paul Scherrer Institut, Villigen, Switzerland

[7] Institute for Biomedical Engineering, University and ETH Zürich, Zürich, Switzerland

Animal model. All the procedures were approved by the Ethical Committee of Canton Vaud, Switzerland (EC 2647.2) and performed according to the guidelines from Directive 2010/63/EU of the European Parliament on the protection of animals used for scientific purposes. Applying the 3R principle (replace, reduce, refine), we used the same animals for a parallel study on abdominal aortic aneurysm formation (yet to be published). The incidence of ascending aneurysms is the same for ApoE $^{-/-}$ and regular C57Bl/6J mice[1], while the incidence of abdominal aortic aneurysms is significantly higher for ApoE $^{-/-}$ mice[2]. Therefore male ApoE $^{-/-}$ mice on a C57Bl/6J background were purchased from Janvier (Saint Berthevin, France). At the age of 12 weeks, n=47 mice were implanted with a 200 µl osmotic pump (model Alzet 2004; Durect Corp, Cupertino, CA), filled with a solution of angiotensin II in saline (Bachem, Bubendorf, Switzerland) as previously described [3]. At the age of 14 weeks, n= 6 control mice were implanted with a 200 µl osmotic pump delivering saline. Each pump infused angiotensin II at 1000 ng/kg/min [4]. Water and regular mouse diet were available *ad libitum* and animals were observed daily after the osmotic pump implantation. Aneurysm onset was instrumentally verified as described later.

Sample size. In total, N= 47 angiotensin II-infused animals and n= 6 controls underwent in vivo imaging. N= 35 out of the 47 angiotensin II-infused animals were included in the long-term in vivo imaging part of the study. N=13 of these animals died with hemothorax (n=7) or hemoabdomen (n=6) during the study. The remaining animals were sacrificed after 10 (n=4), 18 (n=5) and 28 (n=13) days of angiotensin II infusion (Figure 1). These animals were all scanned with ultrasound prior to pump implantation and at each intermediate time point. A subsample (n=11/35) was followed-up with micro-CT at baseline and intermediate time points. Additional micro-CT scans were obtained at intermediate time points if mice from the original micro-CT group died or were sacrificed. This resulted in n=13 micro-CT scans at day10, n=12 at day 18 and n=7 at day 28.
N=12/47 angiotensin II–infused animals were included in the short-term in vivo imaging part of the study. These were sacrificed after 3 days of Ang II infusion. The day 3 animals were all scanned with ultrasound prior to pump implantation and with ultrasound and micro-CT prior to sacrifice. More mice were sacrificed in the short-term study because at this early stage of the disease the differences with controls were expected to be smaller. N=1 animal of this group died with hemothorax after in vivo imaging at day 3, but prior to sacrifice.
In total n=48/53 ascending aortic samples (n=30/33 samples from sacrificed Ang II-infused animals, n=12/14 samples from Ang II-infused animals that succumbed to hemothorax or hemoabdomen, and n=6/6 samples from saline-infused animals) were imaged with PCXTM. Five samples could not be analyzed ex vivo, either because the sample was damaged during dissection (n=3) or because too much time had passed between death from aneurysm rupture and tissue collection (n=2). The operator was blinded during all data analysis.
For ultrasound, micro-CT and PCXTM each animal represents one data point. For image-guided histology a representative, randomized sample of n=4 animals was analyzed at each time point. The goal of image-guided histology was to describe the biological variation within the lesions. If a lesion was visible on PCXTM, image-guided staining targeted 2-3 regions of the lesion in order to capture its start, middle and end. For each animal the final data point represents the mean value of these regions, in order to account for intra-subject variability. If no lesion was visible (e.g. saline-infused controls) 2 regions were analyzed per sample.

In vivo imaging. During both ultrasound and micro-CT imaging, animals were anesthetized with 1.5% isoflurane. Ultrasound imaging was performed with a high-frequency ultrasound device (Vevo 2100, VisualSonics, Toronto, Canada) using a linear array probe (MS 550D, frequency 22-55 MHz). Heart rate and respiration rate were kept constant, and the temperature of the ultrasound table was kept at 40 degrees during the experiment. Blood flow in the ascending aorta was visualized by Color Doppler measurements of the aortic arch and Pulsed Doppler measurements at the level of the ascending aorta (just downstream the aortic valve) and the descending aorta (just distal to the bifurcation of the left subclavian artery). An example of the placement of the Pulsed Doppler probe is shown in Figure Id. Diameter distension waveforms were acquired using radiofrequency (RF) MMode at the ascending aorta, and BMode images of the aortic arch were obtained in longitudinal view. The ultrasound imaging protocol was limited in time for ethical reasons (duration of anesthesia). If measurements did not meet sufficient quality, e.g. due to shadows or reverberations, they were repeated as long as the available time frame permitted so. Images that were still of insufficient quality were excluded from further analysis. Animals followed up in vivo with micro-CT were injected in the lateral tail vein with 4 µl/gram body weight of ExiTron nano 12000 (Miltenyi Biotec, Bergisch Gladbach, Germany) as previously described [5]. After the experiments, mice were anesthetized by Ketamine/Xylazine and the sacrifice was resolved following tissue collection.

PCXTM imaging. After sacrifice, the aorta was flushed in situ by transcardiac perfusion with phosphate buffered saline (PBS, pH 7.4) through the left ventricle. The thoracic aorta was carefully excised and samples were fixated by immersion in freshly prepared 4% paraformaldehyde (PFA) at 4°C temperature for 24 hours. In animals that succumbed to transmural aortic dissection, the aorta was collected (without flushing) as soon as possible after finding them dead. N=48 collected samples were scanned at the TOMCAT beamline of the Swiss Light Source, Paul Scherrer Institut, Villigen, Switzerland. Samples were embedded in 1% agarose gel to stabilize them. The imaging setup consists in two gratings (phase and absorption) with 3.98 and 2 um pitch respectively, positioned at a relative distance of 121 mm. It corresponds to the third fractional Talbot distance at 25 keV. A total of 1441 projections have been acquired over 180 degrees rotations for each of the 5 phase grating steps [5].

Lesion terminology. Throughout the manuscript, a consistent terminology has been used to avoid confusion between different types of lesions that were observed in the aortic wall.
Laminar rupture: a discontinuity of a single elastic aortic lamina (i.e. one of the seven lamellar layers) due to breaks in single lamellar units in the tunica media, as observed on the Miller stain.
Interlaminar hematoma: a local entrapment of free erythrocytes that is confined within the tunica media, between 2 laminae, as observed on the H&E stain.
Dissection (or tear): a discontinuity of the tunica media with a depth of 3 or more consecutive laminae, as observed on the Miller stain. On PCXTM images, dissections were identified as a discontinuity of the tunica media in which the luminal gap corresponds to at least 10% of the wall thickness in an unchanged (normal) area.
Transmural dissection: A full thickness rupture of the aortic wall (including tunica media and tunica adventitia) that leads to hemorrhage and death of the animal by hypovolemic shock.

Image processing. Ultrasound Pulsed Doppler waveforms were traced within a custom-made environment platform in Matlab (Mathworks, Natick, MA) and the average of three different waveforms was computed. The entity of aortic regurgitation in the ascending aorta was subsequently determined as the (dimensionless) ratio of the cumulative integral of negative velocity over the total cumulative integral of positive and negative velocity, both of which were quantified via numerical integration over the flow velocity waveform. A custom-written, Matlab-based application was used to obtain the aortic diameter distension from the 1D RF MMode data. For each diameter measurement, 3 cardiac cycles were selected and plotted as a reference for semi-automatic wall segmentation as previously described [6]. The circumferential cyclic Green-Lagrange strain (eq. 1) was calculated as a measure for aortic compliance under the assumption of uniform strain around the vessel [7].

$$Circ.strain = \frac{1}{2}\left[\left(\frac{D_{sys}}{D_{dia}}\right)^2 - 1\right] * 100\% \qquad \text{(eq. 1)}$$

2D Ultrasound BMode images were analyzed using the built-in Vevo tracing software. Area measurements were measured in a longitudinal view, similar to the method proposed by Rateri *et al* [1]*.* BMode measurements include the ascending aspect of the aorta from (but not including) the aortic valve until (but not including) the branching of the brachiocephalic trunk (Figure 1a, 1b). All reconstructed 3D datasets (in vivo micro-CT as well as PCXTM) were semi-automatically segmented into 3D models using the commercial software package Mimics (Materialise, Leuven, Belgium). Segmentation of the in vivo micro-CT data allowed for quantification of the 3D volume of the pressurized, blood-filled lumen. Volume measurements included the ascending portion of the aorta, just before the branching of the brachiocephalic trunk (Figure 1a, 1b). Segmentation of ex vivo PCXTM data allowed for 3 dimensional quantification of the size of focal dissections. Volume measurements of the dissections quantified the volume of the loss of substance in the tunica media, and thus required extrapolation of the damaged tunica intima (Figure 3a). In order to describe the topography of the circumferential variation of these dissections the ascending aorta was subdivided into 4 quadrants representing the outer convex, left, right and inner convex aspect of the ascending aorta (Figure 3). For each quadrant the total volume of all (parts of) dissections observed in it was computed.

PCXTM-guided histology. After PCXTM scanning, the samples were fixated as mentioned above, processed and embedded in paraffin according to standard histological procedures. 4 µm thick paraffin sections were carefully compared to the corresponding PCXTM images under a Leica DM750 bright field microscope to spot the exact location of dissections. Selected slides were stained with Haematoxylin-Eosin (H&E) to assess general morphology. Miller stain and Sirius red F3B (CI35782, Direct red 80) were combined to specifically highlight elastic fibers and collagen on the same section. Prussian Blue, which is a specific stain for iron, confirmed the cytoplasmic hemoglobin and hemosiderin within macrophages (hemosiderophages) at sites of hematoma resorption. In order to confirm the contribution of smooth muscle cells apoptosis to the progressive degeneration of the media, sections obtained from controls and angiotensin II-infused mice at different time points were co-stained for cleaved caspase 3 and α-SMA on the same slice using the Ventana Discovery XT. Dewaxed and rehydrated paraffin sections were pretreated with heat using the CC1 solution under standard conditions (36 minutes). The primary antibody rabbit anti cleaved caspase-3 (Asp175, Cell Signaling) diluted 1:100 in 1% BSA in PBS was

incubated 1 hour at 37°C. Detection was performed with the secondary rabbit OmniMAp and the DAbMap revelation kit (Roche Diagnostics, Rotkreuz, Switzerland). Antibodies were eluted using heat then the rabbit anti α-SMA (clone E184, Abcam) diluted 1:200 in 1% BSA in PBS was incubated 1 hour at 37°C. After incubation with a donkey α-rabbit biotin antibody diluted 1:500 in 1% BSA in PBS (Jackson ImmunoResearch Laboratories), chromogenic revelation was performed with a BlueMap kit (Roche Diagnostics, Rotkreuz, Switzerland).

Histology image processing. All slides were photographed using an automated slide scanner (VI20-L100, Olympus) and analyzed using a dedicated plug-in in the open source software Fiji [8]. All slides were carefully compared to the stack of 2D PCXTM images as well as the segmented 3D PCXTM vessel in order to determine the orientation of the slide. Each intersection was subsequently subdivided into one of four quadrants. Outer convex, inner convex, left and right aortic quadrants were determined based on the exact match between 2D PCXTM and image-guided histology. Combined thickness of the tunica intima and media as well as thickness of the tunica adventitia were measured on combined SR-Miller stains. In order to account for local variations in thickness, 32 measurements were made for each scanned slide: 4 measurements per quadrant for both the intima-media and the adventitia. Furthermore the number and size (in mm^2) of focal dissections was quantified on SR-Miller stains for each quadrant. Similar to the PCXTM measurements, the size of the lesions was quantified as the area of loss of substance (dissection) in the wall. The number of laminar ruptures was quantified for each elastic layer and for each quadrant on SR-Miller stains. In order to avoid double reporting of data, laminar ruptures that formed part of a focal dissection (i.e. loss of continuity of three consecutive luminal laminae) were not included in the count. Finally, the size of interlaminar hematomas was quantified on Haematoxylin-Eosin (H&E) sections as the area occupied by extraluminal free erythrocytes. This area was computed for each quadrant and outside each lamina. Laminae were ordered from the luminal (L1) to the abluminal (L7) side. If less than 7 laminae were present, no values were counted for L7. If more than 7 laminae were present, results for L8 were added to those of L7. Given the low variation in lamellae in between mice [9], both effects were rare and cancelled each other out. A semi-quantitative measurement of collagen deposition was performed by image analysis (ImageJ). The image was split into its RGB channels and the Green channel was used for image analysis. The aortic wall was segmented manually and the same threshold was used for all analyzed images.

Statistics. For all in vivo experiments the baseline scans (and not the saline-infused control animals) served as control data. All data from in vivo experiments were first transformed from the lognormal to the normal domain by a log transformation. Log-transformed data were tested for normality by the Shapiro-Wilk parametric hypothesis test and visually checked for adherence to the x=y reference line on a normal probability plot. Equal variance was tested with Bartlett's test. The conditions for parametric testing were met for all in vivo variables and therefore their variation in between time points was calculated using a one-way Anova analysis (Table II). Post-hoc pairwise comparisons were performed using a Bonferroni correction. A p-value of 0.05 was considered significant (*), and a p-value of 0.001 was considered highly significant (**).The mean and 95% confidence interval were first calculated in the normal domain and then back-calculated to the original scale. Therefore geometric means and asymmetric confidence intervals are reported in the Figures and Tables.

For the ex vivo experiments (PCXTM and histology), 6 saline-infused mice (and not the baseline data, which were not available ex vivo) served as controls. For the ex vivo measurements we reported the incidence (Table II) and the variation of magnitude within non-zero values (Table I) separately.

Incidence was defined as 100*n1/n2, with n1 all mice that have a non-zero value at that time point (or quadrant, or lamina) and n2 all mice that were measured at that time point (or quadrant, or lamina). Incidence rates were reported as bar plots with 95% confidence intervals. The 95% confidence interval was calculated based on a student`s distribution and SEM=sqrt (p*(1-p)/n). For each analyzed variable the variation of the incidence values in between time points, in between quadrants and in between layers was calculated using a chi-square test (Table II). Pairwise comparisons were performed using a Tukey`s HSD multiple comparisons test. A p-value of 0.05 was considered significant (*), and a p-value of 0.001 was considered highly significant (**).

The non-zero values from ex vivo experiments (PCXTM and histology) had fewer measurements per time point than the in vivo measurements. There were too few samples per time point to ascertain normality and the Bartlett test showed significant differences in variance between time points, even after log transformation. Therefore in this case a Kruskal-Wallis analysis was performed, followed by a post-hoc Dunn`s test for pairwise comparisons. A p-value of 0.05 was considered significant (*), and a p-value of 0.001 was considered highly significant (**). For the analysis of ex vivo data in between circumferential quadrants and in between laminae the conditions for Anova analysis were met and a similar approach as for in vivo data was followed.

References

1. Rateri DL, Davis FM, Balakrishnan A, Howatt DA, Moorleghen JJ, O'Connor WN, Charnigo R, Cassis LA, Daugherty A. Angiotensin ii induces region-specific medial disruption during evolution of ascending aortic aneurysms. *Am. J. Pathol.* 2014;184:2586-2595
2. Trachet B, Fraga-Silva RA, Jacquet P, Stergiopulos N, Segers P. Incidence, mortality and confounding factors for aaa detection in angiotensin ii-infused mice: A meta-analysis. *Cardiovasc. Res.* 2015;108:159-170
3. Trachet B, Renard M, De Santis G, Staelens S, De Backer J, Antiga L, Loeys B, Segers P. An integrated framework to quantitatively link mouse-specific hemodynamics to aneurysm formation in angiotensin ii-infused apoe -/- mice. *Ann. Biomed. Eng.* 2011;39:2430-2444
4. Wang Y, Ait-Oufella H, Herbin O, Bonnin P, Ramkhelawon B, Taleb S, Huang J, Offenstadt G, Combadiere C, Renia L, Johnson JL, Tharaux P-L, Tedgui A, Mallat Z. Tgf-beta activity protects against inflammatory aortic aneurysm progression and complications in angiotensin ii-infused mice. *J. Clin. Invest.* 2010;120:422-432
5. Trachet B, Fraga-Silva RA, Piersigilli A, Tedgui A, Sordet-Dessimoz J, Astolfo A, Van der Donckt C, Modregger P, Stampanoni M, Segers P, Stergiopulos N. Dissecting abdominal aortic aneurysm in ang ii-infused mice: Suprarenal branch ruptures and apparent luminal dilatation. *Cardiovasc. Res.* 2015;105:213-222
6. Trachet B, Fraga-Silva RA, Londono FJ, Swillens A, Stergiopulos N, Segers P. Performance comparison of ultrasound-based methods to assess aortic diameter and stiffness in normal and aneurysmal mice. *PLoS ONE*. 2015;10:e0129007
7. Goergen CJ, Barr KN, Huynh DT, Eastham-Anderson JR, Choi G, Hedehus M, Dalman RL, Connolly AJ, Taylor CA, Tsao PS, Greve JM. In vivo quantification of murine aortic cyclic strain, motion, and curvature: Implications for abdominal aortic aneurysm growth. *J. Magn. Reson. Imaging*. 2010;32:847-858
8. Schindelin J, Arganda-Carreras I, Frise E, Kaynig V, Longair M, Pietzsch T, Preibisch S, Rueden C, Saalfeld S, Schmid B, Tinevez J-Y, White DJ, Hartenstein V, Eliceiri K, Tomancak P, Cardona A. Fiji - an open source platform for biological image analysis. *Nat. Methods*. 2012;9:10.1038/nmeth.2019
9. Goergen CJ, Li H-H, Francke U, Taylor CA. Induced chromosome deletion in a williams-beuren syndrome mouse model causes cardiovascular abnormalities. *J. Vasc. Res.* 2011;48:119-129

Ascending aortic aneurysm in angiotensin II- infused mice: formation, progression and the role of focal dissections

Supplementary Figures and Tables

Bram Trachet[1,2], Alessandra Piersigilli[3,4], Rodrigo A. Fraga-Silva[1], Lydia Aslanidou[1], Jessica Sordet-Dessimoz[5], Alberto Astolfo[6], Marco F.M. Stampanoni[6,7], Patrick Segers[2], Nikolaos Stergiopulos[1]

[1] Institute of Bioengineering, Ecole Polytechnique Fédérale de Lausanne, Lausanne, Switzerland

[2] IBiTech - bioMMeda, Ghent University-iMinds Medical IT, Ghent, Belgium

[3] School of Life Sciences, PTEC GE, Ecole Polytechnique Fédérale de Lausanne, Lausanne, Switzerland

[4] Institute of Animal Pathology, Vetsuisse Faculty, University of Bern, Bern, Switzerland

[5] Histology Core Facility, Ecole Polytechnique Fédérale de Lausanne, Lausanne, Switzerland

[6] Swiss Light Source, Paul Scherrer Institut, Villigen, Switzerland

[7] Institute for Biomedical Engineering, University and ETH Zürich, Zürich, Switzerland

Supplement Material

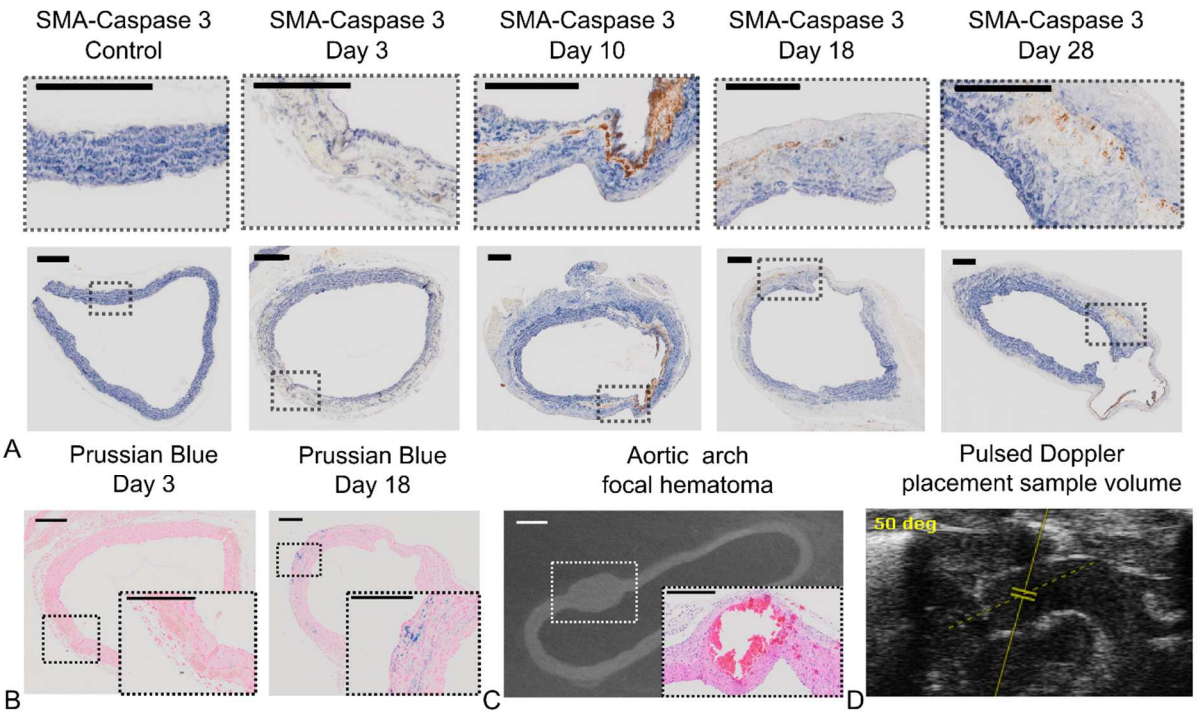

Figure I. Smooth muscle cells apoptosis, hematoma resorption, focal hematoma formation and Pulsed Doppler sample volume placement. a. Combined stain for alpha-actin (smooth muscle cells in blue) and caspase-3 (apoptosis in brown) at different time points. Note that staining for apoptosis occurs at later time points and is more prominent within the dissection area (likely also highlighting necrosis) and its edges. **b**. The Prussian Blue stain at day 18 shows hemosiderophage aggregates (in blue) surrounding and resorbing the hematoma. The stain at day 3 is negative, since the hematoma just occurred. **c**. A focal hematoma in the aortic arch was observed on PCXTM images in 3/47 cases. Image-guided H&E revealed a local bleeding in the outer laminae of the tunica media without any intimal tear. **d.** BMode image demonstrating the placement of the sample volume for Pulsed Doppler measurements in the ascending aorta. Blood flow velocity was measured just distal to the valve, in the direction of the flow.

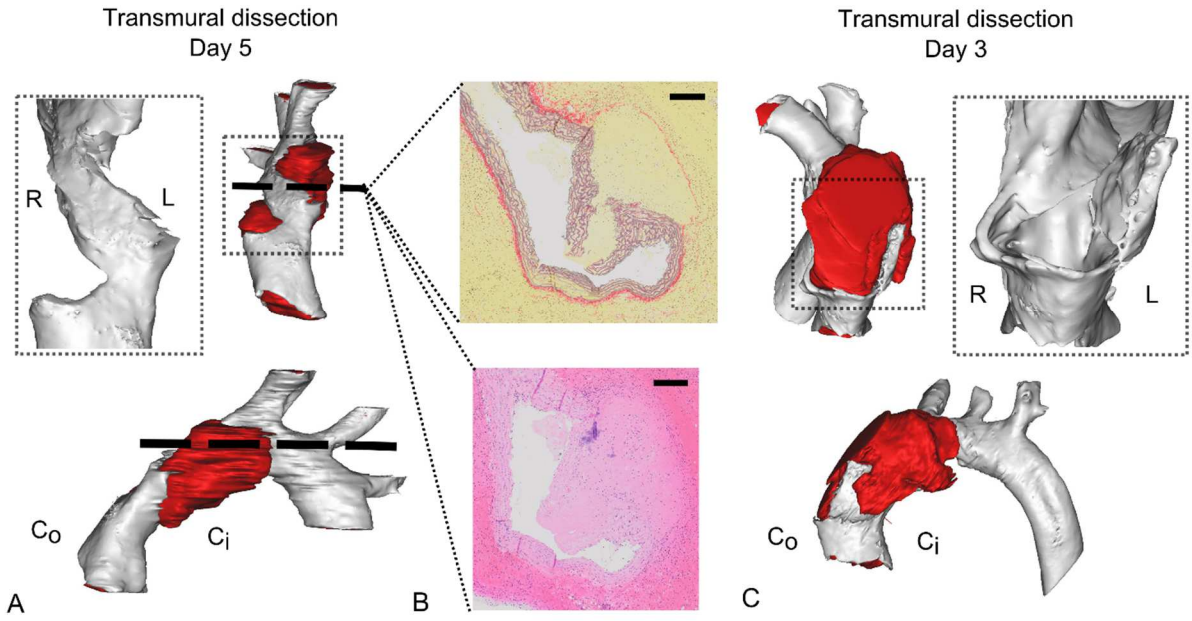

Figure II. Transmural dissection at early time points. a: 3D segmentation based on PCXTM images of the aortic arch of an animal that was found dead with hemothorax after 5 days of angiotensin II infusion. Tunica media in white, coagulated blood (that was flowing out after the media ruptured and before the animal died) in red **b.** PCXTM-guided histology at the location of the aortic dissection. Top: SR-Miller stain showing transmural dissection of all laminae. Notice the still unchanged adventitia. Bottom: H&E stain indicating local acute hemorrhage around the dissection. **c.** 3D segmentation based on PCXTM images of the aortic arch of another animal, that was found dead with hemothorax after 3 days of angiotensin II infusion. Tunica media in white, coagulated blood (that was flowing out after the media ruptured and before the animal died) in red. L: Left, R: right, C_o: outer convex, C_i: inner convex.

In vivo measurements vs time		p	D0	D3	D10	D18	D28
aortic regurgitation (%)	A	**	2.2 [1.4 - 3.5]	5.2 [2.1 - 13.1]	10.8 [7.5 - 15.5]	11.1 [7.4 - 16.6]	10.9 [8.1 - 14.5]
1D Mmode diameter (mm)	A	*	1.8 [1.7 - 1.8]	1.9 [1.8 - 2.0]	1.8 [1.7 - 1.9]	1.8 [1.7 - 2.0]	2.0 [1.8 - 2.1]
2D Bmode area (mm^2)	A	**	6.5 [6.3 - 6.8]	7.9 [7.1 - 8.9]	7.4 [6.9 - 8.0]	8.3 [7.7 - 9.0]	8.7 [7.9 - 9.6]
3d micro-CT volume (mm^3)	A	**	6.4 [5.8 - 7.0]	8.3 [7.3 - 9.4]	10.4 [8.8 - 12.2]	11.7 [9.6 - 14.2]	12.8 [9.0 - 18.2]
circ. Wall strain (%)	A	**	18.6 [16.6 - 20.9]	11.2 [9.6 - 13.0]	11.5 [8.6 - 15.4]	11.2 [8.8 - 14.2]	9.8 [6.5 - 14.9]
Ex vivo measurements vs time			**Ctrl**	**D3**	**D10**	**D18**	**D28**
3D dissection volume (x 10^{-3} mm^3)	K	ns		18.8 [6.8 - 51.9]	30.8 [6.0 - 156.7]	32.5 [11.1 - 95.4]	18.5 [6.2 - 55.1]
media thickness (x 10^{-2} mm)	K	*	7.5 [7.1 - 7.9]	8.8 [7.4 - 10.4]	10.9 [9.6 - 12.4]	11.0 [9.4 - 13.0]	12.6 [10.2 - 15.7]
adventitia thickness (x 10^{-2} mm)	K	*	1.3 [1.2 - 1.4]	3.1 [1.5 - 6.1]	6.6 [41.4 - 10.7]	5.9 [4.9 - 7.2]	5.2 [3.3 - 8.5]
collagen area (mm^2)	K	ns	1.0 [0.7 - 1.5]	0.8 [0.4 - 1.6]	2.0 [0.7 - 6.1]	5.2 [2.7 - 9.9]	3.6 [0.5 - 26.3]
hematoma area (x 10^{-3} mm^2)	K	ns		32.4 [4.6 - 228.7]	1.4 [0.2 - 8.7]	1.0 [0.2 - 7.2]	0.2 [0.2 0.2]
exitron volume (x 10^{-3} mm^3)	K	ns		5.2 [0.6 - 44.0]	2.0 [0.3 - 15.4]		2.5 [1.4 - 4.5]
N laminar ruptures ()	K	*	5.4 [3.7 - 7.8]	16.8 [11.1 - 25.3]	19.0 [9.4 - 38.7]	23.3 [13.3 - 40.9]	24.2 [11.5 - 50.7]
Measurements vs quadrant			**Q1**	**Q2**	**Q3**	**Q4**	
3D dissection volume (x 10^{-3} mm^3)	A	*	25.0 [11.7 - 53.7]	6.2 [2.9 - 13.0]	8.1 [3.7 - 17.8]	12.3 [5.4 - 27.8]	
N laminar ruptures ()	A	ns	3.6 [2.4 - 5.6]	3.9 [2.8 - 5.3]	3.4 [2.5 - 4.6]	3.0 [2.3 - 4.0]	
Measurements vs lamina			**L1**	**L2**	**L3**	**L4**	**L5**	**L6**	**L7**
hematoma area (x 10^{-1} mm^2)	A	*			5.1 [2.4 - 11.0]	8.9 [5.0 - 16.2]	16.3 [9.4 - 28.4]	20.0 [10.0 - 40.2]	14.6 [6.8 - 31.3]
N laminar ruptures ()	A	**	1.7 [1.2 - 2.6]	3.0 [2.2 - 4.0]	3.0 [2.2 - 4.0]	2.8 [2.0 - 4.1]	2.2 [1.7 - 3.0]	1.8 [1.3 - 2.6]	0.8 [0.6 - 1.2]

Table I. Measurement values. Table indicating the non-zero values of both in vivo and ex vivo measurements at each time point (top), for each quadrant (middle) and for each laminar layer (bottom). P-values indicate overall significance (*: $p<0.05$, **: $p<0.001$), while the results of pairwise comparisons are shown in the corresponding Figures. For all variables the mean and the 95% confidence interval were calculated in the normal domain (after a log transformation) but reported in the original scale, resulting in geometric means and asymmetric confidence intervals. A: One-way Anova analysis after log transformation. K: Kruskal-Wallis analysis (performed when conditions for Anova were not met).

In vivo incidence per time point	p	D0	D3	D10	D18	D28
aortic regurgitation (%)	ns	95.5 ± 6.3	100 ± 0.0	100 ± 0.0	100 ± 0.0	92.9 ± 14.8
Ex vivo incidence per time point		**Ctrl**	**D3**	**D10**	**D18**	**D28**
PCXTM dissection volume (%)	**	0.0 ± 0.0	92.3 ± 16.0	66.7 ± 35.5	100 ± 0.0	100 ± 0.0
hematoma area (%)	**	0.0 ± 0.0	75.0 ± 60.1	100.0 ± 0.0	100.0 ± 0.0	25.0 ± 60.1
exitron volume (%)	*	0.0 ± 0.0	63.6 ± 31.9	40.0 ± 56.3	0.0 ± 0.0	37.5 ± 39.5
N laminar ruptures (%)	ns	100 ± 0.0	100 ± 0.0	100 ± 0.0	100 ± 0.0	100 ± 0.0
Incidence per quadrant		**Q1**	**Q2**	**Q3**	**Q4**	
PCXTM dissection volume (%)	*	48.6 ± 16.6	50.0 ± 16.4	55.3 ± 16.3	23.7 ± 14.0	
N laminar ruptures (%)	ns	95.5 ± 9.2	95.5 ± 9.2	100 ± 0.0	95.5 ± 9.2	

Incidence per lamina		L1	L2	L3	L4	L5	L6	L7
hematoma area (%)	**	0.0 ± 0.0	0.0 ± 0.0	22.7 ± 18.5	36.4 ± 21.3	45.5 ± 22.0	40.9 ± 21.7	36.4 ± 21.3
N laminar ruptures (%)	**	86.4 ± 15.2	100 ± 0.0	95.5 ± 9.2	86.4 ± 15.2	95.5 ± 9.2	86.4 ± 15.2	54.5 ± 22.0

Table II. Measurement incidences. Table indicating the incidence of both in vivo and ex vivo measurements for each time point (top), for each quadrant (middle) and for each laminar layer (bottom). Incidence was defined as 100*n1/n2, with n1 all mice that had a non-zero value at that time point (or quadrant, or lamina) and n2 all mice that were measured or analyzed at that time point (or quadrant, or lamina). For each variable the overall p-value of the chi square test on the incidence proportions is shown (*: $p<0.05$, **: $p<0.001$). The results of pairwise comparisons are shown in the corresponding Figures.